Optimum Third Current Harmonic During Nondead Zone and Its Control Implementation to Improve PF for DCM Buck PFC Converter

Kai Yao, *Member, IEEE*, Xufeng Zhou, Fei Yang, *Member, IEEE*, Siwen Yang, Cheng Cao, and Chunyan Mao

***Abstract*—A buck power factor correction (PFC) converter is widely used in low-power applications for its high efficiency in the entire universal input voltage range. However, because of the inherent dead zone, the input power factor (PF) is not high. A buck PFC converter operating in a discontinuous conduction mode is introduced. When the duty cycle is constant during the line cycle, the input current contains a large amount of negative third harmonic, especially at a low input voltage. By proposing an optimum third harmonic injection during the nondead zone and its control implementation, a higher PF and a lower output voltage ripple within the entire universal input voltage range are achieved. The experimental verifications are carried out on a 120-W prototype with universal input.**

***Index Terms*—Discontinuous conduction mode (DCM), optimum third current harmonic, power factor correction (PFC).**

I. Introduction

ELECTRONIC and electrical devices are widely used in production and daily life, and accompanying with the improvement and convenience, also comes a harmonic pollution, which results in several problems such as voltage distortion, heating, noise, etc. So, various kinds of power factor correction (PFC) techniques are proposed to reduce the harmonics and meet the regulation standards [1], [2].

Buck, boost, flyback, etc. can be used as a PFC converter. The Buck topology is chosen in low-power applications for its high efficiency in universal input, especially at a low line input [3]–[8]. Moreover, a Buck converter gains a low dc output voltage, a low voltage stress of the switch clamped to a line voltage, and an electrolytic capacitor with a low voltage rating [9]–[11].

A buck PFC converter has large harmonics distortions and a low input power factor (PF) for it cannot regulate an input current into a pure sinusoid due to its inherent dead zone. Some methods with different operation modes are proposed to improve the performance of the Buck PFC converter. Huber *et al.* [6] present a very significant optimization, design-oriented analysis, and performance evaluation on a clamped-current buck PFC converter. Wu *et al.* [10] analyze the constant on-time control of a critical conduction mode (CRM) buck converter, which reduces the input current harmonics and improves PF; Xie *et al.* [11] add an auxiliary switch and two diodes so as to eliminate the dead zone; Zeng and Zang [12] obtain a higher PF and efficiency within the whole universal input voltage range by optimizing the peak current reference; Wu *et al.* [13] introduce a variable on-time controller into a CRM Buck PFC front-end converter in high-brightness light-emitting diode applications to reduce the current harmonics and meet the limitations of a lighting system; Lu and Ki [14] put forward a light-load power loss reduction scheme and analyzes an example of a Buck PFC and Buck–Boost dc/dc single-stage converter; Ohnuma and Itoh [15] adopt an active buffer with a small capacitor for power decoupling in a Buck PFC converter and achieves a low output voltage ripple and a high PF; For an interleaved Buck PFC converter, Yang *et al.* [16] investigate a DSP implementation of the adaptive slope compensation in a clamping current mode control. Yao *et al.* [17] propose a variable duty cycle control scheme for discontinuous conduction mode (DCM) Boost PFC converter to make the input current contain only the third harmonic in phase with the fundamental component.

This paper introduces a Buck PFC converter working in a DCM. By analyzing its operation principle, it is clear that the form of the input current with a constant duty cycle control is as the same as a sinusoidal function subtracted by a constant value, which can be called sinusoidal current control (SCC). The Fourier analysis shows that the negative third harmonic accounts for the most part of harmonics of SCC. Thus, a method of an optimum third current harmonic control (OTCHC) and its implementation is proposed to reduce current distortions and improve PF. Section II analyzes the working principle of the DCM Buck PFC converter and deduces the input current and PF in detail. Section III proposes the OTCHC and specifies the control implementation. Section IV compares the proposed OTCHC with SCC in terms of PF, harmonics, output voltage ripple, as well as peak and root-mean-square (RMS) value of inductor current. Section V shows the design example and the experimental results.

Manuscript received October 7, 2016; revised December 20, 2016; accepted January 18, 2017. Date of publication January 25, 2017; date of current version August 2, 2017. This work was supported in part by the National Natural Science Foundation of China (51677091), in part by the Excellent Youth Fund Project of Jiangsu Natural Science Foundation (BK20160086), and in part by the Six Talents Peak Project of Jiangsu Province (XNY-033). Recommended for publication by Associate Editor D. G. Lamar.

The authors are with the School of Automation, Nanjing University of Science and Technology, Nanjing 210094, China (e-mail: yaokai@njust.edu.cn; 13770836879@163.com; carryyangs@gmail.com; 314414414@qq.com; 735953810@qq.com; 1095859615@qq.com).

Color versions of one or more of the figures in this paper are available online at http://ieeexplore.ieee.org.

Digital Object Identifier 10.1109/TPEL.2017.2657883

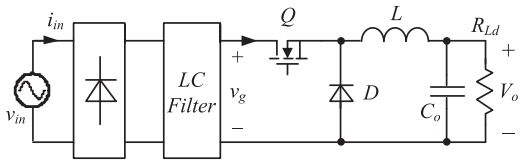

Fig. 1. Power circuit of a Buck PFC converter.

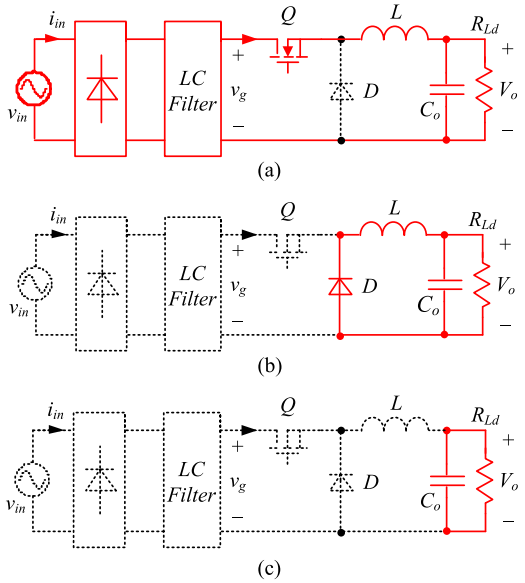

Fig. 2. Equivalent circuits. (a) Switching pattern 1 (b) Switching pattern 2 (c) Switching pattern 3.

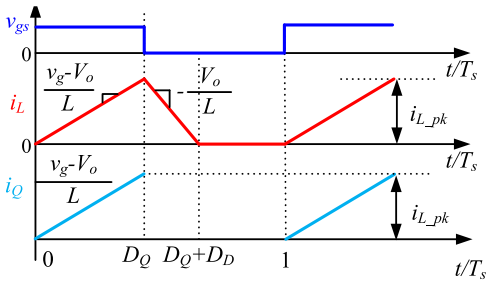

Fig. 3. Waveform of inductor and switch current in a switching cycle.

II. Working Principle of DCM Buck PFC Converter

Fig. 1 shows the power circuit of a Buck PFC converter, where V_o is the output voltage. The input voltage and the rectified voltage v_g can be defined, respectively, as

$$v_{\rm in} = V_m \sin \omega t \tag{1}$$

$$v_g = V_m \left|\sin \omega t\right| \tag{2}$$

where V_m and ω are the amplitude and angular frequency of the input voltage, respectively.

The Buck converter has three kinds of switching patterns during one switching cycle when the inductor current works in a DCM. The corresponding equivalent circuits, the waveform of the inductor, and switch currents in a switching cycle are depicted in Figs. 2 and 3.

1) *Switching Pattern* 1

As shown in Fig. 2(a), when Q is ON, L, C_o, and $R_{\rm Ld}$ conduct, and the KVL equation is

$$v_g - L di_L/dt = V_o. \tag{3}$$

Then, the rising slope of the inductor current is derived as

$$di_L/dt = (v_g - V_o)/L. \tag{4}$$

When Q turns OFF, the inductor current reaches its peak value, which is

$$i_{L\_\rm pk} = (V_m \left|\sin \omega t\right| - V_o)\, D_Q / L f_s \tag{5}$$

where D_Q is the duty cycle and f_s is the switching frequency.

2) *Switching Pattern* 2

As shown in Fig. 2(b), when Q is off, L, C_o, $R_{\rm Ld}$, and D conduct, and the KVL equation is

$$V_o + L di_L/dt = 0. \tag{6}$$

Thus, the falling slope of the inductor current is

$$di_L/dt = -V_o/L. \tag{7}$$

The inductor current reaches zero before Q turns on again in the next switching cycle, and the corresponding duty cycle of this falling period is

$$D_D = \frac{i_{L\_\rm pk} f_s}{V_o/L} = (V_m \left|\sin \omega t\right| - V_o)\, D_Q / V_o. \tag{8}$$

3) *Switching Pattern* 3

The inductor current is zero during this period, and the output load is supplied only by the output capacitor. The corresponding equivalent circuit is shown in Fig. 2(c).

From above, the average current of the switch in a switching cycle can be expressed as

$$i_{Q\_\rm av} = \frac{1}{2} i_{L\_\rm pk} D_Q = \frac{(V_m \left|\sin \omega t\right| - V_o)\, D_Q^2}{2 L f_s}. \tag{9}$$

During $[0,\ \pi]$, the input current can be given directly as

$$i_{\rm in} = i_{Q\_\rm av}. \tag{10}$$

The Buck converter works when v_g is higher than V_o. Thus, the input current in half of a line cycle is

$$i_{\rm in} = \begin{cases} 0 & 0 < \omega t < \theta \\ \dfrac{D_Q^2 V_o\,(a\left|\sin \omega t\right| - 1)}{2 L f_s} & \theta \le \omega t \le \pi - \theta \\ 0 & \pi - \theta < \omega t < \pi \end{cases} \tag{11}$$

where $a = V_m/V_o$, and $\theta = \arcsin(1/a)$.

According to the aforementioned analysis, when D_Q is constant in half of a line cycle, the switch current waveform as well as its peak and average value are shown in Fig. 4.

The average input power and the input PF can be written as

$$P_{\rm in} = \frac{1}{\pi} \int_0^{\pi} v_{\rm in} i_{\rm in}\, d\omega t \tag{12}$$

$$\mathrm{PF} = \frac{P_{\rm in}}{S} = \frac{\frac{1}{\pi}\int_0^{\pi} v_{\rm in} i_{\rm in}\, d\omega t}{\frac{1}{\sqrt{2}} V_m I_{\rm in\_rms}} \tag{13}$$

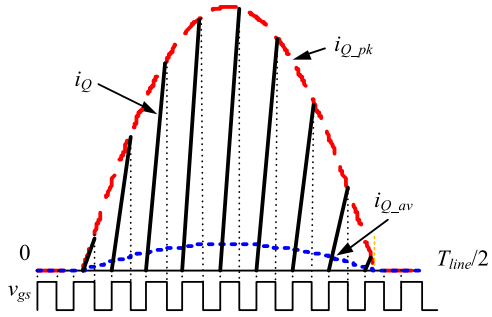

Fig. 4. Switching current waveform in half of a line cycle.

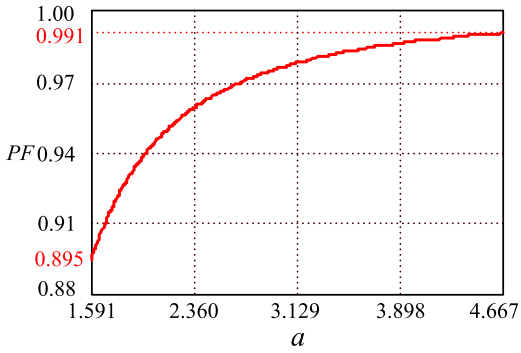

Fig. 5. Relationship between input PF and a.

where $I_{\text{in\_rms}}$ is the RMS value of the input current.

Substitution of (1) and (11) into (12) yields

$$P_{\text{in}} = \frac{V_m D_Q^2}{2\pi L f_s} \int_{\theta}^{\pi-\theta} \sin\omega t \left(V_m \left|\sin\omega t\right| - V_o\right) d\omega t. \quad (14)$$

Assuming that the efficiency of the converter is 100%, the duty cycle is

$$D_Q = \sqrt{\frac{2\pi L f_s P_o}{V_m \int_{\theta}^{\pi-\theta} \sin\omega t \left(V_m \left|\sin\omega t\right| - V_o\right) d\omega t}}. \quad (15)$$

Combining (11) and (15) yields

$$i_{in} = \begin{cases} 0 & 0 < \omega t < \theta \\ \dfrac{\pi P_o \left(V_m \left|\sin\omega t\right| - V_o\right)}{V_m \int_{\theta}^{\pi-\theta} \sin\omega t \left(V_m \left|\sin\omega t\right| - V_o\right) d\omega t} & \theta \le \omega t \le \pi - \theta \cdot \\ 0 & \pi - \theta < \omega t < \pi \end{cases} \quad (16)$$

Using (13) and (16) leads to

$$\text{PF} = \frac{\sqrt{\frac{2}{\pi}} \int_{\theta}^{\pi-\theta} \sin\omega t \left(a\left|\sin\omega t\right| - 1\right) d\omega t}{\sqrt{\int_{\theta}^{\pi-\theta} \left(a\left|\sin\omega t\right| - 1\right)^2 d\omega t}}. \quad (17)$$

Fig. 5 shows the input PF obtained from (17). It can be seen that PF increases with a. PF is only 0.895 when $a = 90\sqrt{2}/80$. Therefore, it is necessary to put forward a new method to improve PF.

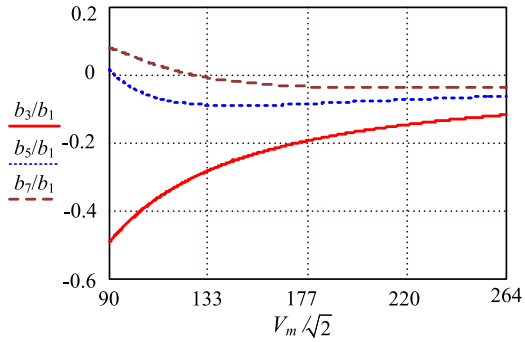

Fig. 6. Normalized amplitudes of the third, fifth, and seventh harmonics of SCC.

III. Optimum Third Current Harmonic to Improve Power Factor

A. Proposal of OTCHC

In order to get a higher PF during the universal input, the harmonics should be analyzed first. By Fourier analysis, the input current harmonics can be expressed as

$$I_n = \frac{2}{\pi} \int_0^{\pi} i_{\text{in}} \cdot \sin n\omega t d\omega t \; (n = 1, 3, 5, \ldots). \quad (18)$$

The normalized amplitudes of the third, fifth, and seventh harmonics to the base of the fundamental component are depicted in Fig. 6. As shown in (11), during $[\theta, \pi - \theta]$, the input current is in form as the same as a sinusoidal function subtracted by a constant value, however, there is no input current during $[0, \theta]$ and $[\pi - \theta, \pi]$. Therefore, the third, fifth, seventh, and higher order harmonics are produced when the input current is analyzed by the Fourier equation. From Fig. 6, the negative third one covers the most part of harmonics. Hence, during $[\theta, \pi - \theta]$, if the current is introduced with some amounts of the positive third harmonic subtracted by a constant value, as shown in (19), the harmonic will be reduced and PF will be improved

$$i_{\text{in}} = \begin{cases} 0 & 0 < \omega t < \theta \\ I_1 \left[\left(\sin\omega t - \sin\theta\right) \right. & \\ \quad \left. + I_3^* \left(\sin 3\omega t - \sin 3\theta\right)\right] & \theta \le \omega t \le \pi - \theta \\ 0 & \pi - \theta < \omega t < \pi \end{cases} \quad (19)$$

where I_1 is the amplitude of the fundamental component, and I_3^* is the normalized amplitude of the third harmonic.

Substitution of (1) and (19) into (12) leads to

$$P_{\text{in}} = \frac{V_m I_1}{4\pi} \left[2\pi - 4\theta - 2\sin 2\theta - 3I_3^* \left(2\sin 2\theta + \sin 4\theta\right)\right]. \quad (20)$$

Assuming that the efficiency of the converter is 100%, i.e., $P_{\text{in}} = P_o$, thus, we can get I_1 as

$$I_1 = \frac{4\pi P_o}{V_m \left[2\pi - 4\theta - 2\sin 2\theta - 3I_3^* \left(2\sin 2\theta + \sin 4\theta\right)\right]}. \quad (21)$$

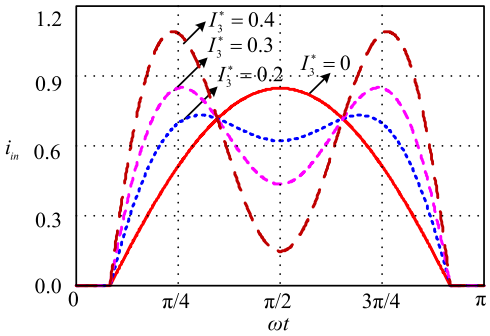

Fig. 7. Input currents with different values of I_3^* in half of a line cycle.

Substitution of (1), (19), and (21) into (13) yields

$$\mathrm{PF} = \frac{1}{2\sqrt{2\pi \int_{\theta}^{\pi-\theta} \left[\frac{(\sin\omega t - \sin\theta) + I_3^*(\sin 3\omega t - \sin 3\theta)}{2\pi - 4\theta - 2\sin 2\theta - 3I_3^*(2\sin 2\theta + \sin 4\theta)}\right]^2 d\omega t}}. \tag{22}$$

Fig. 7 shows the input currents with different values of I_3^* under a 220 VAC input voltage. It can be seen that the input current gets a local minimum at $\pi/2$, which is different along with the change of I_3^*. It should be noted that the input current during $[0, \pi]$ should be no less than zero, i.e.

$$I_1\left[\left(\sin\frac{\pi}{2} - \sin\theta\right) + I_3^*\left(\sin\frac{3\pi}{2} - \sin 3\theta\right)\right] \geq 0. \tag{23}$$

Then

$$I_3^* \leq \frac{1}{(1+2\sin\theta)^2}. \tag{24}$$

According to the parameters of the converter given in Section V, the range of I_3^* is

$$0 \leq I_3^* \leq 0.49. \tag{25}$$

The input PF is depicted in Fig. 8 according to (22), where PF is variable and dependent on a and I_3^*. Differentiating (22) with respect to I_3^* and setting it to zero, the relationship between the optimum I_3^* and θ can be expressed as (26) shown at the bottom of this page.

From (26) and $\theta = \arcsin(1/a)$, Fig. 9 can be depicted.

Combining (11) and (19), in order to obtain such an input current, the duty cycle should be variable as

$$D_Q = \sqrt{\frac{2Lf_sI_1}{V_o}} \cdot \sqrt{\frac{(|\sin\omega t| - \sin\theta) + I_{3\_\mathrm{opt}}^*(|\sin 3\omega t| - \sin 3\theta)}{a|\sin(\omega t)| - 1}}. \tag{27}$$

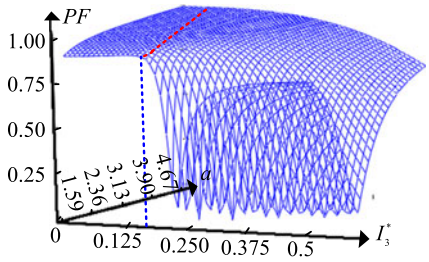

(a)

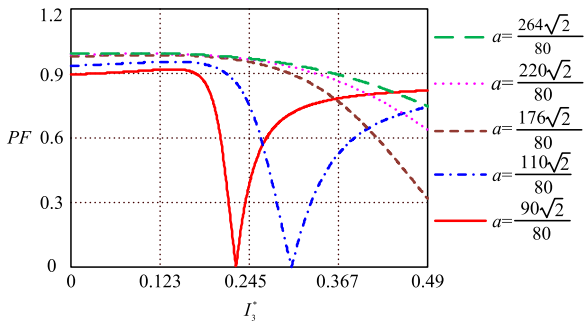

(b)

Fig. 8. Relationship between input PF and a as well as I_3^*. (a) Surface of PF as a function of a and I_3^*. (b) Curves of PF at different I_3^* for a certain value of a.

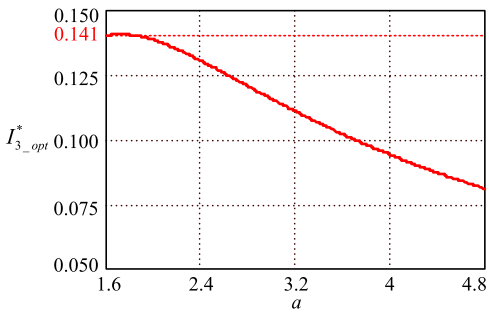

Fig. 9. Relationship between optimum I_3^* and a.

Defining $y = |\sin\omega t|$, (27) can be expressed as

$$D_Q = \sqrt{\frac{2Lf_sI_1}{V_o}} \cdot \sqrt{\frac{\left(y - \frac{1}{a}\right) + I_{3\_\mathrm{opt}}^*\left(y(3-4y^2) - \frac{1}{a}\left(3 - \frac{4}{a^2}\right)\right)}{ay - 1}}. \tag{28}$$

Expanded by the Taylor series at the deployment point of y_0 and capturing the first two items, (28) can be written as

$$D_{Q\_\mathrm{approx}} \approx D_0 \cdot (1 - My) \tag{29}$$

$$I_{3\_\mathrm{opt}}^* = -\frac{4\sin\theta\sin 3\theta(\pi-2\theta)^2 + \frac{8}{3}\sin\theta\cos\theta\left(13\sin^2\theta - 6\sin^4\theta - 1\right)(\pi-2\theta) + \frac{4}{3}\sin^2 2\theta\left(14\sin^2\theta - 17\right)}{2(\cos 6\theta - 2)(\pi-2\theta)^2 + 4\sin 2\theta\left(2 - 17\sin^2\theta + 26\sin^4\theta - 8\sin^6\theta\right)(\pi-2\theta) + 2\sin^2 2\theta\left(37 - 76\sin^2\theta + 36\sin^4\theta\right)} \tag{26}$$

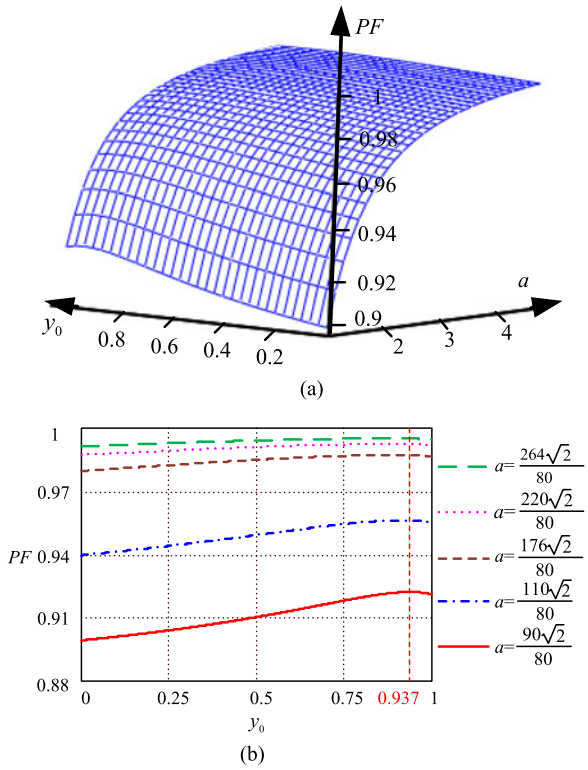

Fig. 10. PF surface and curves (a) Surface of PF as a function of a and y_0 (b) Input PF with different y_0 for different a.

where D_0 and M can be obtained as

$$D_0 = \sqrt{\frac{2Lf_sI_1}{V_o}} \cdot \sqrt{\frac{\left(4I_{3\_\text{opt}}^* - 3a^2I_{3\_\text{opt}}^* - a^2 + 2ay_0I_{3\_\text{opt}}^*\right)^2}{a^3\left[a^2\left(1+3I_{3\_\text{opt}}^* - 4y_0^2I_{3\_\text{opt}}^*\right) - 4I_{3\_\text{opt}}^*\left(1+ay_0\right)\right]}} \tag{30}$$

$$M = \frac{4a^2y_0I_{3\_\text{opt}}^* + 2aI_{3\_\text{opt}}^*}{\left(1+3I_{3\_\text{opt}}^*\right)a^2 - \left(4I_{3\_\text{opt}}^* + 2ay_0I_{3\_\text{opt}}^*\right)}. \tag{31}$$

From (1), (11), (13), and (29), the input PF can be derived as

$$\text{PF} = \frac{\sqrt{\frac{2}{\pi}}\int_\theta^{\pi-\theta}\sin\omega t(a\left|\sin\omega t\right|-1)(1-M\left|\sin\omega t\right|)^2d\omega t}{\sqrt{\int_\theta^{\pi-\theta}\left(a\left|\sin\omega t\right|-1\right)^2(1-M\left|\sin\omega t\right|)^4d\omega t}}. \tag{32}$$

Fig. 10(a) shows the surface of the input PF according to (32) and Fig. 10(b) shows PF with different y_0 and a. It can be clearly seen that when $y_{0\_\text{opt}} = 0.937$, there comes the highest PF for each a.

Substitution of $y_{0\_\text{opt}} = 0.937$ and (26) into (31) leads to a complex mathematical expression, and to simplify the analysis,

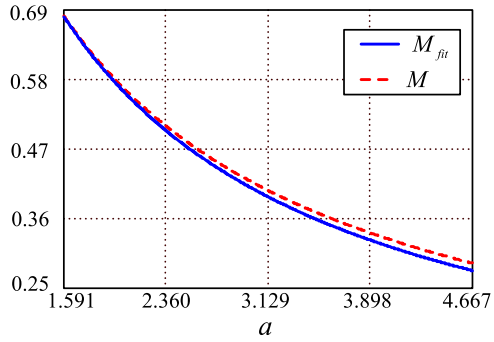

Fig. 11. Relationship between M and a.

the expression is plotted in Fig. 11. A further analysis reveals that the relationship between M and a is similar to an inverse proportional function as

$$M_{\text{fit}} = \frac{k_1}{a+k_2} \tag{33}$$

where $k_1 = 1.446$ and $k_2 = 0.536$.

Thus, D_Q can be rewritten as

$$\begin{aligned} D_{Q\_\text{fit}} &= D_1\left(1 - \frac{k_1}{a+k_2}\left|\sin\omega t\right|\right) \\ &= D_1\left(\frac{V_m + k_2V_o - k_1V_o\left|\sin(\omega t)\right|}{V_m + k_2V_o}\right). \end{aligned} \tag{34}$$

According to (1), (11), (12), and (34), we can get

$$\begin{aligned} P_o = P_{\text{in}} = \frac{V_mD_1^2}{2\pi Lf_s}\int_\theta^{\pi-\theta}&\left[\sin\omega t\cdot\left(V_m\left|\sin\omega t\right| - V_o\right)\right. \\ &\left.\cdot\left(\frac{V_m + k_2V_o - k_1V_o\left|\sin(\omega t)\right|}{V_m + k_2V_o}\right)^2\right]d\omega t. \end{aligned} \tag{35}$$

Thus, the expression of D_1 can be derived as (36) shown at bottom of this page.

The relative errors between (27), (29), and (34) are defined as

$$\Delta E_1 = \frac{D_Q - D_{Q\_\text{approx}}}{D_Q} \tag{37}$$

$$\Delta E_2 = \frac{D_Q - D_{Q\_\text{fit}}}{D_Q}. \tag{38}$$

Combining (27), (29)–(31), (34) and (37)–(38), Fig. 12 can be plotted. It indicates that the maximum error is about 10% and it occurs at the junction point of the dead zone and the nondead zone, around which the input power accounts for a little proportion of the whole transmitted power. And, the minimum error is near zero and takes place at $\pi/2$, around which the input power occupies the majority of the power. Therefore, the control

$$D_1 = \sqrt{\frac{2\pi Lf_sP_o}{V_m\int_\theta^{\pi-\theta}\sin\omega t\cdot\left(V_m\left|\sin\omega t\right| - V_o\right)\left(\frac{V_m + k_2V_o - k_1V_o\left|\sin(\omega t)\right|}{V_m + k_2V_o}\right)^2d\omega t}} \tag{36}$$

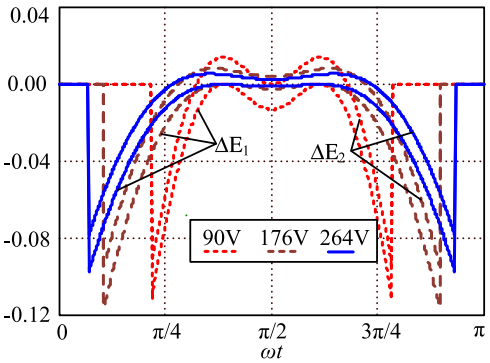

Fig. 12. Relative error between duty cycles.

error between the ideal duty cycle and the fitted one is small and acceptable.

B. Implementation of Control Circuit

Fig. 13 shows the control circuit schematic. R_1 and R_2 compose a voltage divider with a voltage ratio k_s to sense the rectified input voltage v_g, so $v_A = k_s V_m |\sin\omega t|$. The circuit consists of D_1, C_1, R_3, and R_4 is used to obtain the peak value of v_A, i.e., $v_B = k_s V_m$. R_5 and R_6 compose a voltage divider to sense the output voltage, and the voltage sensor ratio is deliberately set to make $v_{\rm of} = 1.446\,kV_o$. Let $R_{10} = R_{11}$, $R_7 = 0.371\,R_{11}$ and $R_9 = 0.742\,R_8$, then $v_E = k_s(V_m + k_2 V_o)$. Let $R_{12} = R_{13} = R_{14} = R_{15}$, then $v_D = k_s(V_m + k_2 V_o - k_1 V_o|\sin\omega t|)$. The voltage divider consists of R_{16}, R_{17} samples v_o to compare with $V_{\rm ref}$, R_{18} and C_2 compose the compensation network, and $v_{\rm EA}$ is the output of the error amplifier. v_D, $v_{\rm EA}$, and v_E are connected with v_x, v_y and v_z, respectively, and $v_P = v_{\rm EA}(V_m + k_2 V_o - k_1 V_o|\sin\omega t|)/(V_m + k_2 V_o)$, which is sent to the pulse width modulation control IC UC3525A and compared with the sawtooth wave. In this way, the duty cycle in (35) can be realized and the coefficient D_1 is determined by $v_{\rm EA}$ and the amplitude of the sawtooth. It should be noted that

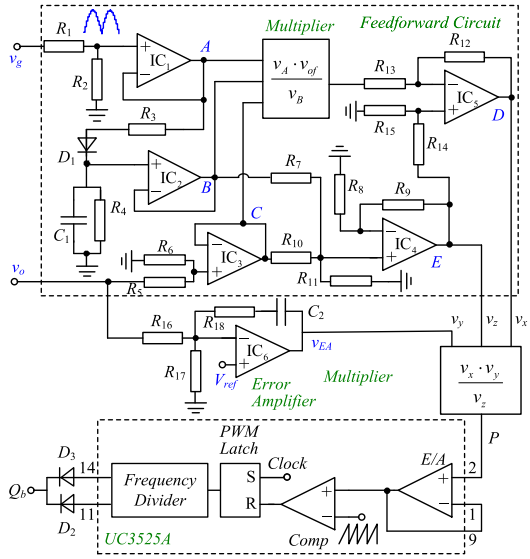

Fig. 13. Control circuit schematic.

the output capacitance has a big influence on the effect of the proposed method, for a higher ripple voltage follows as a result of decreasing capacitance.

IV. Performance Comparison

A. Comparison of Input PF and Current Harmonics

Combining (11), (34), and (36) yields the expression of the input current as (39) shown at the bottom of this page.

According to (16) and (39), the theoretical input current waveforms of the converter of SCC and OTCHC at 90, 176, and 264 VAC input voltages are depicted in Fig. 14.

Substituting (33) into (32), the input PF of OTCHC can be obtained, as depicted in Fig. 15, which also shows the PF curve of SCC from Fig. 5. Obviously, OTCHC achieves a higher PF than SCC.

According to (11), (18), and (39), the normalized amplitudes of the third, fifth, and seventh harmonics to the base of the

$$i_{\rm in} = \begin{cases} 0 & 0 < \omega t < \theta \\ \dfrac{\pi P_o \left(V_m |\sin\omega t| - V_o\right)\left(1 - \dfrac{k_1 V_o |\sin(\omega t)|}{V_m + k_2 V_o}\right)^2}{V_m \int_\theta^{\pi-\theta} \sin\omega t \cdot \left(V_m |\sin\omega t| - V_o\right)\left(1 - \dfrac{k_1 V_o |\sin(\omega t)|}{V_m + k_2 V_o}\right)^2 d\omega t} & \theta \le \omega t \le \pi - \theta \\ 0 & \pi - \theta < \omega t < \pi \end{cases} \tag{39}$$

$$p^*_{\rm in\_1} = \frac{v_{\rm in} i_{\rm in}}{P_o} = \frac{\pi \sin\omega t \left(V_m |\sin\omega t| - V_o\right)}{\int_\theta^{\pi-\theta} \sin\omega t \left(V_m |\sin\omega t| - V_o\right) d\omega t}$$

$$p^*_{\rm in\_2} = \frac{v_{\rm in} i_{\rm in}}{P_o} \tag{40a}$$

$$= \frac{\pi \sin\omega t \cdot \left(V_m |\sin\omega t| - V_o\right)\left(V_m + k_2 V_o - k_1 V_o |\sin\omega t|\right)^2}{\int_{\theta_0}^{\pi-\theta_o} \sin\omega t \cdot \left(V_m |\sin\omega t| - V_o\right)\left(V_m + k_2 V_o - k_1 V_o |\sin\omega t|\right)^2 d\,\omega t} \tag{40b}$$

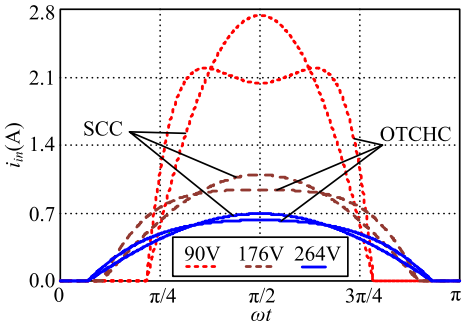

Fig. 14. Theoretical input current waveforms.

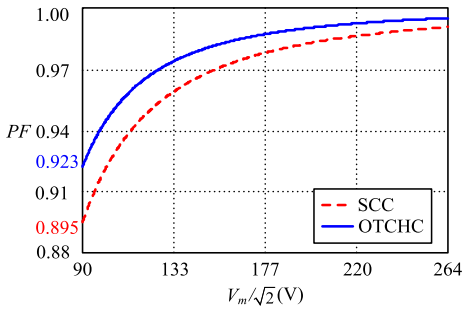

Fig. 15. Input PF of converter of OTCHC and SCC.

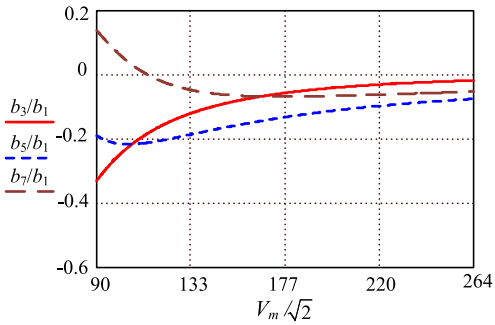

Fig. 16. Normalized amplitudes of the third, fifth, and seventh harmonics of OTCHC.

fundamental component are depicted in Fig. 16. Comparing Fig. 16 with Fig. 6, it is clear that the third harmonic is greatly reduced within the entire input voltage range, and the fifth and seventh harmonics are increased.

B. Comparison of Output Voltage Ripple

From (1), (16), and (39), the normalized instantaneous input power of SCC and OTCHC can be expressed as equation (40a) and (40b) as shown at previous page.

Under a 90 VAC input voltage, (40a) and (40b), shown at the bottom of the previous page, can be plotted in half of a line cycle, as shown in Fig. 17. The output capacitor is used to balance the difference between the instantaneous input power and output power. When $p^*_{\text{in}} > 1$, the storage capacitor C_o is charged, and when $p^*_{\text{in}} < 1$, C_o is discharged. t_1 and t_2, are the time instants when $p^*_{\text{in\_1}}$ and $p^*_{\text{in\_2}}$ crosses 1 for SCC and OTCHC, respectively. The normalized energy discharging C_o

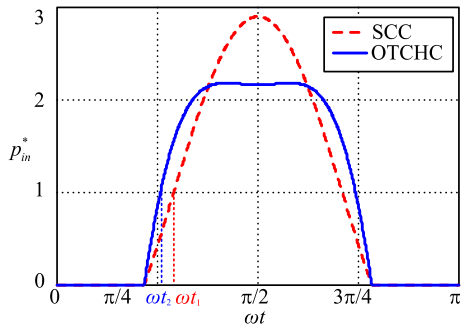

Fig. 17. Normalized instantaneous input power in half of a line cycle.

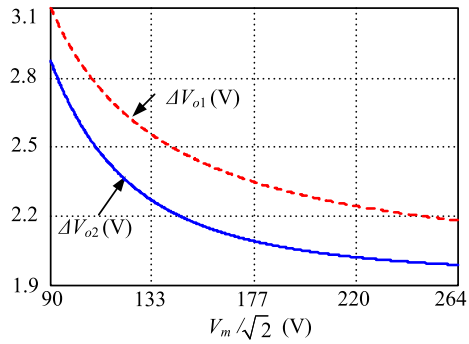

Fig. 18. Curves of output voltage ripples.

equals the charged energy in half of a line cycle. The relationship between the crossing time instants and V_m are shown in (41)

$$\omega t_1 = -4.551\cdot 10^{-12}\cdot\left(\frac{V_m}{\sqrt{2}}\right)^5 + 4.44\cdot 10^{-9}\cdot\left(\frac{V_m}{\sqrt{2}}\right)^4 - 1.723\cdot 10^{-6}\cdot\left(\frac{V_m}{\sqrt{2}}\right)^3 + 3.345\cdot 10^{-4}\cdot\left(\frac{V_m}{\sqrt{2}}\right)^2 - 3.29\cdot 10^{-2}\cdot\left(\frac{V_m}{\sqrt{2}}\right) + 2.1571 \quad (41a)$$

$$\omega t_2 = -7.881\cdot 10^{-12}\cdot\left(\frac{V_m}{\sqrt{2}}\right)^5 + 7.79\cdot 10^{-9}\cdot\left(\frac{V_m}{\sqrt{2}}\right)^4 - 3.048\cdot 10^{-6}\cdot\left(\frac{V_m}{\sqrt{2}}\right)^3 + 5.902\cdot 10^{-4}\cdot\left(\frac{V_m}{\sqrt{2}}\right)^2 - 5.644\cdot 10^{-2}\cdot\left(\frac{V_m}{\sqrt{2}}\right) + 2.8617. \quad (41b)$$

The output voltage ripples of SCC and OTCHC are derived as

$$\Delta V_{o1} = \frac{2P_o\int_0^{t_1}(1-P^*_{\text{in\_1}})dt}{C_oV_o} \quad (42a)$$

$$\Delta V_{o2} = \frac{2P_o\int_0^{t_2}(1-P^*_{\text{in\_2}})dt}{C_oV_o} \quad (42b)$$

Fig. 18 shows ΔV_{o1} and ΔV_{o2} according to (42) and the parameters of the converter. It can be seen that a lower voltage

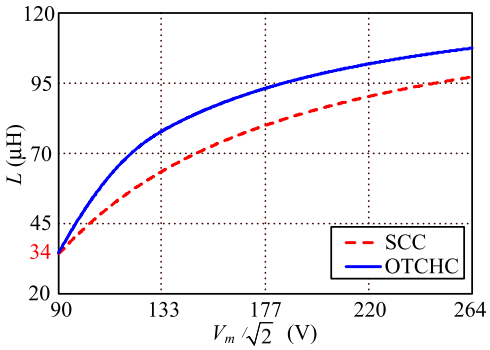

Fig. 19. Critical inductances of OTCHC and SCC.

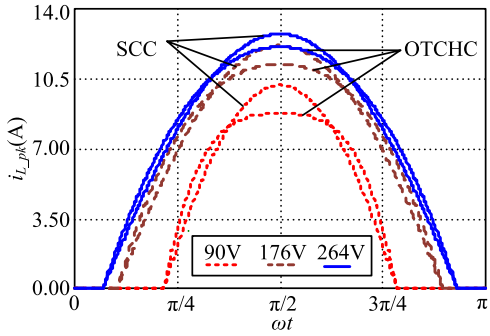

Fig. 20. Peak values of inductor currents of SCC and OTCHC.

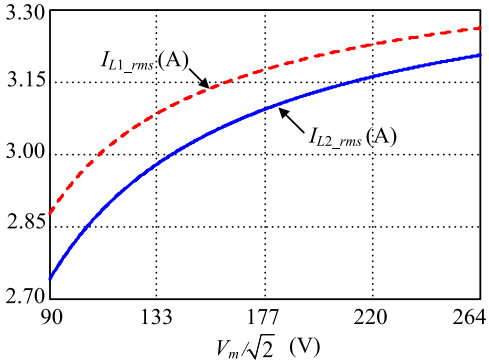

Fig. 21. RMS values of inductor currents of OTCHC and SCC.

ripple of the converter of OTCHC is realized under each input voltage, compared with that of SCC.

C. Comparison of Critical Inductance and Inductor Current

From Fig. 3, DCM means that the inductor current reduces to zero before Q turns ON. So to work in DCM, a PFC converter must meet a condition listed below

$$D_Q + D_D \le 1. \tag{43}$$

According to (8), (15), (34), and (36), the critical inductances of SCC and OTCHC are obtained, respectively, as

$$L_1 \le \frac{V_o^2 \int_\theta^{\pi-\theta} \sin\omega t \left(V_m \left|\sin\omega t\right| - V_o\right) d\omega t}{2\pi f_s P_o V_m \left(\left|\sin\omega t\right|\right)^2} \tag{44a}$$

$$L_2 \le \frac{V_o^2 \int_\theta^{\pi-\theta} \sin\omega t \cdot \left(V_m \left|\sin\omega t\right| - V_o\right)\left(1 - M_{\text{fit}} \left|\sin\omega t\right|\right)^2 d\omega t}{2\pi f_s P_o V_m \left|\sin\omega t\right|^2 \left(1 - M_{\text{fit}} \left|\sin\omega t\right|\right)^2}. \tag{44b}$$

So the critical inductances of SCC and OTCHC can be derived as (45a) and (45b) shown at bottom of this page.

Fig. 19 shows the critical inductances of SCC and OTCHC according to (45) and the converter parameters, which shows that both critical inductances are nearly 34 μH. The following analysis and experimental prototype choose $L_1 = L_2 = 25\,\mu$H out of consideration for a margin.

According to (5), (15), (34), and (36), the peak values of inductor currents of SCC and OTCHC under different input voltages can be depicted in Fig. 20, which shows that OTCHC obtains a lower value around $\pi/2$ and a higher value around θ and $\pi - \theta$.

The RMS value of the inductor current in a switching cycle and in half of a line cycle can be expressed, respectively, as

$$\begin{aligned} i_{Lb\_\text{rms}} &= \sqrt{\frac{1}{T_s}\int_0^{T_s} i_{Lb}^2 dt} \\ &= \sqrt{\frac{D_Q^3 V_m \left|\sin\omega t\right| \left(V_m \left|\sin\omega t\right| - V_o\right)^2}{3L^2 {f_s}^2 V_o}} \end{aligned} \tag{46}$$

$$\begin{aligned} I_{L\_\text{rms}} &= \sqrt{\frac{2}{T_{\text{line}}}\int_0^{\frac{T_{\text{line}}}{2}} i_{L\_\text{rms}}^2 dt} \\ &= \sqrt{\frac{1}{\pi}\int_\theta^{\pi-\theta} \frac{D_Q^3 V_m \left|\sin\omega t\right| \left(V_m \left|\sin\omega t\right| - V_o\right)^2}{3L^2 f_s^2 V_o} d\omega t}. \end{aligned} \tag{47}$$

Substituting (15) where $L_1 = 25\,\mu$H, (34) and (36) where $L_2 = 25\,\mu$H into (47), respectively, the RMS value of the

$$L_1 = \frac{V_o^2 \int_\theta^{\pi-\theta} \sin\omega t \left(V_m \left|\sin\omega t\right| - V_o\right) d\omega t}{2\pi f_s P_o V_m} \tag{45a}$$

$$L_2 = \begin{cases} \dfrac{8M_{\text{fit}}^2 V_o^2 \int_\theta^{\pi-\theta} \sin\omega t \cdot \left(V_m \left|\sin\omega t\right| - V_o\right)\left(1 - M_{\text{fit}} \left|\sin\omega t\right|\right)^2 d\omega t}{\pi f_s P_o V_m} & M_{\text{fit}} \ge 0.5 \\ \dfrac{V_o^2 \int_\theta^{\pi-\theta} \sin\omega t \cdot \left(V_m \left|\sin\omega t\right| - V_o\right)\left(1 - M_{\text{fit}} \left|\sin\omega t\right|\right)^2 d\omega t}{2\pi f_s P_o V_m \left(1 - M_{\text{fit}}\right)^2} & M_{\text{fit}} < 0.5 \end{cases} \tag{45b}$$

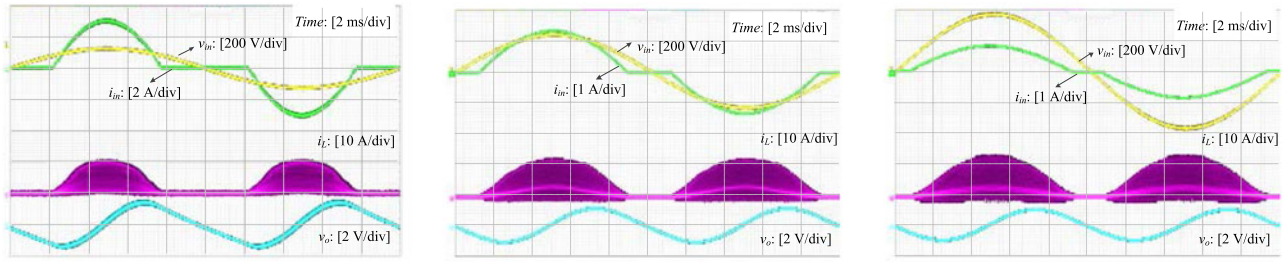

Fig. 22. Experimental waveforms of input voltage, input current, inductor current, and output voltage ripple of SCC (a) 90 VAC (b) 176 VAC (c) 264 VAC.

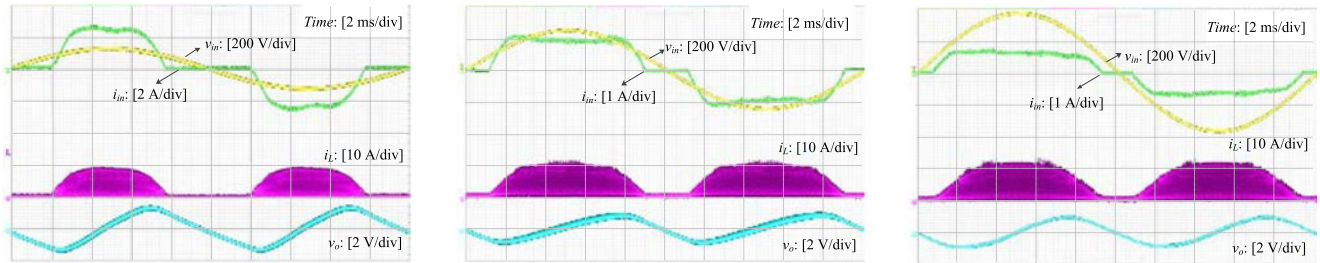

Fig. 23. Experimental waveforms of input voltage, input current, inductor current, and output voltage ripple of OTCHC. (a) 90 VAC. (b) 176 VAC. (c) 264 VAC.

inductor current can be obtained, as shown in Fig. 21, which shows that OTCHC achieves a slightly lower value under each input voltage.

V. Design Example and Experimental Results

A DCM Buck PFC converter prototype has been built and tested to verify the validity of the proposed control method. The parameters are as follows: input voltage: $v_{\rm in}$ = 90-264 VAC/ 50 Hz; output voltage: V_o = 80 VDC; output power: P_o = 120 W; switching frequency: f_s = 100 kHz; Buck inductor: $L_1 = L_2 = 25\,\mu$H; output filter capacitor C_o = 2460 μF.

The experimental waveforms of $v_{\rm in}$, $i_{\rm in}$, i_L, and v_o at a 90, 176, and 264 VAC input voltage are shown in Figs. 22 and 23, respectively, for both methods. It is clear that the input current is not sinusoidal because of the dead zone and a higher input voltage means a smaller dead zone. The peak and RMS value of the input current decrease with the increase of the input voltage, whereas it is the opposite for the inductor current. Compared with SCC, OTCHC changes the input current waveform during $[\theta, \pi - \theta]$, and thus, improves PF. The output voltage ripple of the converter of OTCHC is reduced compared with that of SCC.

The experimental results accord with that in Figs. 14, 18, and 20.

The recorded PF is shown in Fig. 24. As seen, OTCHC realizes a higher PF, and PF increases with the input voltage.

The tested output voltage ripple is shown in Fig. 25, which obviously shows that a larger input voltage results in a lower ripple and the ripple of the converter of OTCHC is reduced compared with that of SCC.

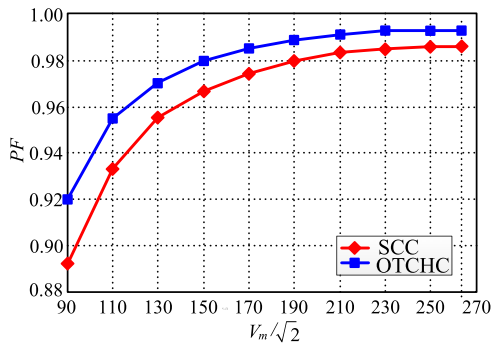

Fig. 24. Experimental results of PF.

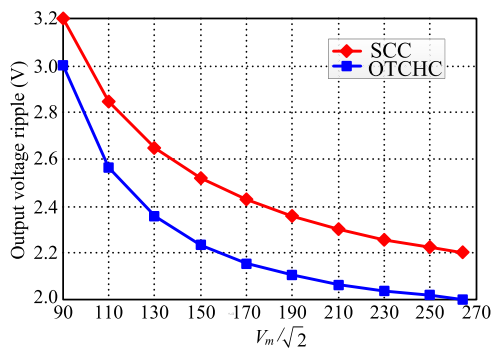

Fig. 25. Experimental results of output voltage ripple.

Fig. 26 depicts the measured efficiency curves, which indicates that the efficiency of the converter of OTCHC is slightly higher than that of SCC. The reason is as follows. From the

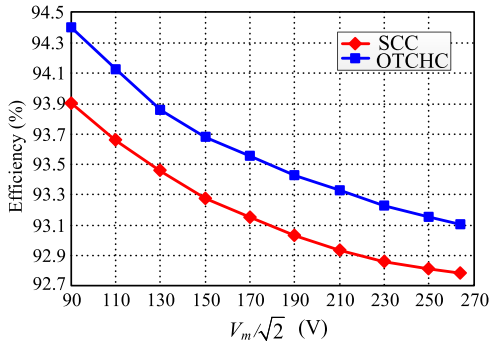

Fig. 26. Experimental results of efficiency.

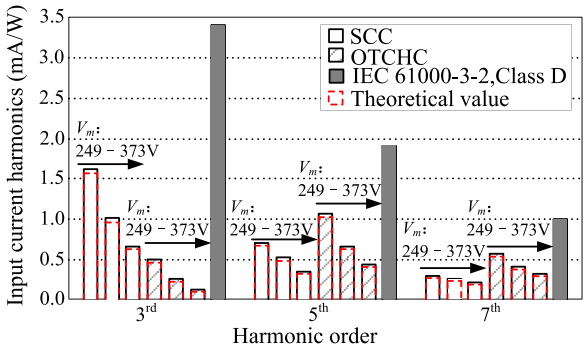

Fig. 27. Theoretical and experimental results of third, fifth, and seventh harmonics.

curves of the inductor current's peak value illustrated in Fig. 20, it can be judged that OTCHC gains a lower value around $\pi/2$ and a higher value around θ and $\pi - \theta$, as far as the turn-OFF loss of the switch and the core loss of the inductor are concerned. Furthermore, it can be seen from Fig. 21 that OTCHC brings about a lower RMS value of the inductor current, compared with that of SCC, thus, the conduction loss is reduced.

Fig. 27 shows the experimental results of the third, fifth, and seventh input current harmonics at 176, 220, and 264 input voltages of both SCC and OTCHC, and the theoretical values got from (18) and (39). It can be seen that the IEC 61000-3-2 Class D standard is met and OTCHC greatly reduces the third harmonic, and increases the fifth and seventh harmonics.

VI. Conclusion

This paper proposes a kind of OTCHC for a DCM Buck PFC converter. The input current, PF, harmonics, output voltage ripple, and the peak and RMS value of the inductor have been deeply analyzed. The experimental results from a 120 W universal input example prove the accuracy of theoretical analysis and the applicability of the proposal method. Compared with SCC, the proposed control method obtains a larger PF and a lower output voltage ripple within the entire universal input voltage range.

References

[1] O. Garcia, J. A. Cobos, R. Prieto, P. Alou, and J. Uceda, "Single phase power factor correction: A survey," *IEEE Trans. Power Electron.*, vol. 18, no. 3, pp. 749–755, May 2003.

[2] B. Singh, B. N. Singh, A. Chandra, K. Al-Haddad, A. Pandey, and D. P. Kothari, "A review of single-phase improved power quality ac-dc converters," *IEEE Trans. Ind. Electron.*, vol. 50, no. 5, pp. 962–981, Oct. 2003.

[3] H. Endo, T. Yamashita, and T. Sugiura, "A high-power-factor buck converter," in *Proc. IEEE Power Electron. Spec. Conf.*, Jun. 1992, pp. 1071–1076.

[4] G. Spiazzi, "Analysis of buck converters used as power factor preregulators," in *Proc. IEEE Power Electron. Spec. Conf.*, Jun. 1997, pp. 564–570.

[5] B. Chen, Y. Xie, F. Huang, and J. Chen, "A novel single-phase buck PFC converter based on one-cycle control," in *Proc. CES/IEEE Int. Power Electron. Motion Control Conf.*, Aug. 2006, pp. 1–5.

[6] L. Huber, G. Liu, and M. M. Jovanovic, "Design-oriented analysis and performance evaluation of buck PFC front end," *IEEE Trans. Power Electron.*, vol. 25, no. 1, pp. 85–94, Jan. 2010.

[7] J. Yang, J. Zhang, X. Wu, Z. Qian, and M. Xu, "Performance comparison between buck and boost CRM PFC converter," in *Proc. IEEE Control Model Power Electron.*, Jun. 2010, pp. 1–5.

[8] C. Hangseok, "Interleaved boundary conductionmode (BCM) buck power factor correction (PFC) converter," *IEEE Trans. Power Electron.*, vol. 28, no. 6, pp. 2629–2634, Jun. 2013.

[9] K. Hirachi and M. Nakaoka, "Improved control strategy on buck type PFC converter," *IET Electron. Lett.*, vol. 34, no. 12, pp. 1162–1163, Jun. 1998.

[10] X. Wu, J. Yang, J. Zhang, and M. Xu, "Design considerations of soft switched buck PFC converter with constant on-time (COT) control," *IEEE Trans. Power Electron.*, vol. 26, no. 11, pp. 3144–3152, Nov. 2011.

[11] X. Xie, C. Zhao, L. Zheng, and S. Liu, "An improved buck PFC converter with high power factor," *IEEE Trans. Power Electron.*, vol. 28, no. 5, pp. 2277–2284, May 2013.

[12] H. Zeng and J. Zhang, "An improved control scheme for buck PFC converter for high efficiency adapter application," in *Proc. IEEE Energy Convers. Congr. Expo.*, Sep. 2012, pp. 4569–4576.

[13] X. Wu, J. Yang, J. Zhang, and Z. Qian, "Variable on-time (VOT) controlled critical conduction, mode buck PFC converter for high input AC/DC HB-LED lighting application," *IEEE Trans. Power Electron.*, vol. 27, no. 11, pp. 3144–3152, Nov. 2012.

[14] D. D.-C. Lu and S.-K. Ki, "Light-load efficiency improvement in buck-derived single-stage single-switch PFC converters," *IEEE Trans. Power Electron.*, vol. 28, no. 5, pp. 2105–2110, May 2013.

[15] Y. Ohnuma and J. Itoh, "A novel single-phase buck PFC AC-DC converter with power decoupling capability using an active buffer," *IEEE Trans. Ind. Appl.*, vol. 50, no. 3, pp. 1905–1914, May/Jun. 2014.

[16] C. Yang, Y. Liu, P. Tseng, T. Pan, H. Chiu, and Y. Lo, "DSP-based interleaved buck power factor corrector with adaptive slope compensation," *IEEE Trans. Ind. Electron.*, vol. 62, no.8, pp. 4665–4677, Aug. 2015.

[17] K. Yao, W. Hu, Q. Li, and J. Lyu, "A novel control scheme of DCM boost PFC converter," *IEEE Trans. Power Electron.*, vol. 30, no. 10, pp. 5605–5615, Oct. 2015.

Kai Yao (M'14) was born in Jiangsu Province, China, in 1980. He received the B.S. degree in industrial automation from Nantong University, Nantong, China, the M.S. degree in mechanical design and theory, and Ph.D. degree in electrical engineering from Nanjing University of Aeronautics and Astronautics, Nanjing, China, in 2002, 2005, and 2010 respectively.

In 2011, he joined the Faculty of Electrical Engineering, School of Automation, Nanjing University of Science and Technology, where he has been engaged in teaching and research in the field of power electronics. His main research interests include power factor correction converters, renewable energy generation system and power supplies for LED.

Xufeng Zhou was born in Henan Province, China, in 1990. He received the B.S. degree in electrical engineering and automation from Shangqiu Normal University, Shangqiu, China, in 2013. He is currently working toward the M.S. degree in power electronics from Nanjing University of Science and Technology.

His research interest focuses on power factor correction converters.

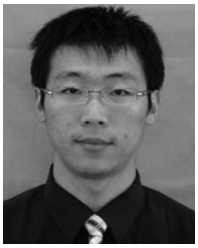

Siwen Yang was born in Fujian Province, China, in 1992. He received the B.S. degree in electrical engineering and automation from Jiangsu University, Zhenjiang, China, in 2015. He is currently working toward the M.S. degree in power electronics from Nanjing University of Science and Technology, Nanjing, China.

His main research interest focuses on power factor correction converters.

Fei Yang (M'16) was born in Shanxi, China, in 1983. He received the B.S. and Ph.D. degrees in electrical engineering from the Nanjing University of Aeronautics and Astronautics, Nanjing, China, in 2006 and 2013, respectively.

From February 2014 to September 2015, he worked as a Postdoctoral Researcher in the Department of Mechanical Engineering in Katholieke Universiteit Leuven, Belgium. Then, he joined the Faculty of Electrical Engineering, School of Automation, Nanjing University of Science and Technology in October 2015, and has been involved in teaching and research in the field of power electronics. His main research interests include power factor correction converters, electromagnetic interference filter design, dc/dc converters, and pulse power generator for micro-EDM.

Dr. Yang has been reviewers of the IEEE TRANSACTIONS ON INDUSTRIAL ELECTRONICS and the IEEE TRANSACTIONS ON POWER ELECTRONICS since 2014 and 2011, respectively.

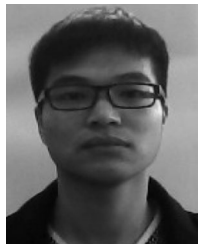

Cheng Cao was born in Jiangsu Province, China, in 1992. He received the B.S. degree in electrical engineering and automation from Yancheng Institute of Technology, Yancheng, China, in 2015. He is currently working toward the M.S. degree in power electronics from Nanjing University of Science and Technology, Nanjing, China.

His main research interest focuses on power factor correction converters.

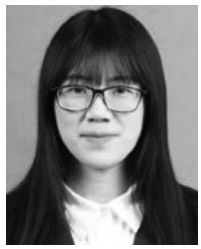

Chunyan Mao was born in Jiangsu Province, China, in 1994. She received the B.S. degree in electrical engineering and automation from Nanjing Normal University, Nanjing, China, in 2016. She is currently working toward the M.S. degree in electrical engineering from Nanjing University of Science and Technology, Nanjing, China.

Her main research interest focuses on power factor correction converters.